



## **MMS Measurements and Modeling of Peculiar Electromagnetic Ion Cyclotron Waves**

Justin H. Lee, Drew L. Turner, Sergio Toledo-Redondo, Sarah K. Vines, Robert C. Allen, Stephen A. Fuselier, Yuri V. Khotyaintsev, Ian J. Cohen, Barry H. Mauk, Christopher T. Russell, et al.

### **► To cite this version:**

Justin H. Lee, Drew L. Turner, Sergio Toledo-Redondo, Sarah K. Vines, Robert C. Allen, et al.. MMS Measurements and Modeling of Peculiar Electromagnetic Ion Cyclotron Waves. *Geophysical Research Letters*, 2019, 46, pp.11,622-11,631. <10.1029/2019GL085182>. <insu-03674391>

**HAL Id: insu-03674391**

**<https://insu.hal.science/insu-03674391v1>**

Submitted on 20 May 2022

**HAL** is a multi-disciplinary open access archive for the deposit and dissemination of scientific research documents, whether they are published or not. The documents may come from teaching and research institutions in France or abroad, or from public or private research centers.

L'archive ouverte pluridisciplinaire **HAL**, est destinée au dépôt et à la diffusion de documents scientifiques de niveau recherche, publiés ou non, émanant des établissements d'enseignement et de recherche français ou étrangers, des laboratoires publics ou privés.



Copyright - All rights reserved

# Geophysical Research Letters

## RESEARCH LETTER

10.1029/2019GL085182

### Key Points:

- Convection flows enabled direct measurement of comprehensive plasma composition during observations of EMIC waves with peculiar properties
- Single-spacecraft and multispacecraft measurements were applied to modeling and tests of linear kinetic theory
- The multiple heavy ion populations, even with low abundances, help sustain wave growth and explain the wave properties

### Supporting Information:

- Supporting Information S1

### Correspondence to:

J. H. Lee,  
justin.h.lee@aero.org

### Citation:

Lee, J. H., Turner, D. L., Toledo-Redondo, S., Vines, S. K., Allen, R. C., Fuselier, S. A., et al. (2019). MMS measurements and modeling of peculiar electromagnetic ion cyclotron waves. *Geophysical Research Letters*, 46, 11,622–11,631. <https://doi.org/10.1029/2019GL085182>















Received 27 AUG 2019

Accepted 15 OCT 2019

Accepted article online 25 OCT 2019

Published online 3 NOV 2019

## MMS Measurements and Modeling of Peculiar Electromagnetic Ion Cyclotron Waves

Justin H. Lee<sup>1</sup> , Drew L. Turner<sup>1</sup> , Sergio Toledo-Redondo<sup>2</sup> , Sarah K. Vines<sup>3</sup> , Robert C. Allen<sup>3</sup> , Stephen A. Fuselier<sup>4</sup> , Yuri V. Khotyaintsev<sup>5</sup> , Ian J. Cohen<sup>3</sup> , Barry H. Mauk<sup>3</sup> , Christopher T. Russell<sup>6,7</sup> , Craig J. Pollock<sup>8</sup> , Robert E. Ergun<sup>9</sup> , Per-Arne L. Lindqvist<sup>10</sup> , and James L. Burch<sup>4</sup> 

<sup>1</sup>The Aerospace Corporation, El Segundo, CA, USA, <sup>2</sup>Institut de Recherche en Astrophysique et Planetologie (IRAP), Toulouse, France, <sup>3</sup>The Johns Hopkins University Applied Physics Laboratory, Laurel, MD, USA, <sup>4</sup>Southwest Research Institute, San Antonio, TX, USA, <sup>5</sup>Swedish Institute of Space Physics (IRFU), Uppsala, Sweden, <sup>6</sup>Institute of Geophysics and Planetary Physics, University of California, Los Angeles, CA, USA, <sup>7</sup>Department of Earth, Planetary, and Space Sciences, University of California, Los Angeles, CA, USA, <sup>8</sup>Goddard Space Flight Center, National Aeronautics and Space Administration, Greenbelt, MD, USA, <sup>9</sup>Laboratory for Atmospheric and Space Physics, University of Colorado, Boulder, CO, USA, <sup>10</sup>KTH Royal Institute of Technology, Stockholm, Sweden

**Abstract** Orbiting Earth's dayside outer magnetosphere on 29 September 2015, the Magnetospheric Multiscale (MMS) satellites measured plasma composition, simultaneous electromagnetic ion cyclotron waves, and intermittent fast plasma flows consistent with ultralow frequency waves or convection. Such flows can accelerate typically unobservable low-energy plasma into a measurable energy range of spacecraft plasma instrumentation. We exploit the flow occurrence to ensure measurement of cold ion species alongside the hot particles—consisting of ionospheric heavy ions and solar wind He<sup>++</sup>—during a subinterval of wave emissions with spectral properties previously described as peculiar. Through application of the composition and multisatellite wave vector data to linear theory, we demonstrate the emissions are in fact consistent with theory, growing naturally in the He<sup>++</sup> band with sufficient free energy.

**Plain Language Summary** Electromagnetic ion cyclotron waves are a special class of plasma waves observed in space near Earth or in other magnetized plasmas. They emit electromagnetic energy near the local ion cyclotron frequencies, a relationship that has been studied extensively through theory. But investigations in space via satellite observations have been hindered by an observational problem. Spacecraft charge positive in sunlight due to interactions between sunlight and spacecraft surfaces. Because of this, positively charged ion species with very low energy are invisible to spacecraft plasma instruments. These invisible low-energy ions are critical to measure to fully understand their effects on the wave emissions. Luckily, electric fields induced by sudden ambient magnetic field changes sometimes provide extra acceleration to these low-energy ions, helping them enter plasma instrument apertures and be observed. We investigate the electromagnetic waves during one such acceleration interval and use comprehensive plasma instrument measurements to show waves thought to be peculiar are instead behaving consistent with theory. Exploring other times and regions of space under similar measurement conditions may improve our understanding of how the electromagnetic waves are generated and their evolution in space and time.

## 1. Introduction

Electromagnetic ion cyclotron (EMIC) waves are observed throughout Earth's magnetosphere (e.g., Allen et al., 2015; Anderson et al., 1992; Le et al., 2001; Min et al., 2012) and in other astrophysical locations (Russell, Wei, et al., 2016). EMIC waves are driven unstable by an anisotropic energetic ion free energy source, often assumed protons due to their abundance, and grow as a parallel-propagating, left-hand circularly polarized mode (Gary et al., 2012). Plasma composition strongly influences EMIC wave growth and propagation (Chen et al., 2011; Lee et al., 2012; Omid et al., 2013; Silin et al., 2011). The waves may also contribute to loss of highly energetic electrons (Thorne & Kennel, 1971; Usanova et al., 2014; Shprits et al., 2016, 2017). Although there have been many studies on ion cyclotron waves, mysteries remain.

Peculiar EMIC waves exist in the dayside magnetosphere from dawn to near noon magnetic local time (MLT), where they may emit at frequencies above the local  $\text{He}^+$  cyclotron frequency and have linear or right-handed polarization, contradicting expectations. Anderson et al. (1992, Anderson, Denton, Ho, et al., 1996) and Denton et al. (1992) used limited plasma composition measurements to study such waves, noting that abnormally high hot proton anisotropy was needed for growth. Similar statistical wave properties were identified by the THEMIS (Time History of Events and Macroscale Interactions during Substorms; Angelopoulos, 2008) satellites, renewing interest in these waves (Min et al., 2012). Plasma composition was inferred from THEMIS ion spectrometer data and applied to investigate similar peculiar EMIC waves; suggesting involvement of a substantial fraction of ionospheric heavy ions ( $\text{He}^+$  and  $\text{O}^+$ ; Lee & Angelopoulos, 2014a, 2014b). But without fully measured plasma composition data, the mystery continued.

This letter discusses EMIC waves with similar peculiar properties observed in the outer dayside magnetosphere by NASA Magnetospheric Multiscale (MMS) mission (Burch et al., 2016) satellites. We combine enhanced MMS measurement capabilities with experience detecting cold ions during plasma flows to characterize cold and energetic ion composition in unprecedented detail. The comprehensive composition data are applied to demonstrate the waves behaved consistent with theory but with lower hot proton anisotropy and heavy ion abundance than suggested in the past work.

## 2. Observations and Analysis

EMIC waves were observed by MMS in the dayside ( $\sim 15$  MLT) outer magnetosphere on 29 September 2015. The MLT sector near noon is a location where dawnside and duskside EMIC wave and plasma properties may be mixed (Lee & Angelopoulos, 2014a, 2014b; Min et al., 2012). The wave properties identified by MMS were more consistent with statistical dawnside waves (Min et al., 2012). Analysis focused on the interval 14:43:10–14:46:50 UT when specific plasma measurement conditions were satisfied at the same time wave emissions were seen.

### 2.1. Particles

Figure 1 shows Fast Plasma Investigation Dual Ion Spectrometers (FPI/DIS; Pollock et al., 2016) and Hot Plasma Composition Analyzer (HPCA; Young et al., 2016) measurements, in which arc signatures consistent with cold ions accelerated by plasma flows (cf. André & Cully, 2012; Chen & Moore, 2004; Lee & Angelopoulos, 2014b; Sauvaud et al., 2001) are seen in the energy flux data at energies below  $\sim 1$  keV, particularly in the FPI/DIS and HPCA  $\text{H}^+$  panels (Figures 1a and 1b). The Absolute Flux Method (AFM; Lee & Angelopoulos, 2014b) detected the presence of cold ions, that is, intervals in energy-time spectrogram data when low-energy ( $< \sim 100$  eV) particle energy fluxes exceed smoothed background fluxes in that same energy range. Intervals labeled 1.0 or “Yes” in Figure 1f indicate times the convection energy (velocity)  $0.5m_p^*|v_{\text{perp}}|^2$  (where  $m_p$  is proton mass and  $v_{\text{perp}}$  (Figure 1g) is the bulk velocity magnitude perpendicular to the average field) exceeds the sum of the minimum energy of the HPCA ( $\sim 1$  eV) and spacecraft potential energy ( $\sim 4$  eV) during the interval; derived from electric field double probes, EDPs; Ergun et al., 2016; Lindqvist et al., 2016) at the same time the AFM was satisfied by presence of enhanced low-energy plasma fluxes. Small changes in total  $\text{O}^+$  and  $\text{He}^+$  density coinciding with the AFM interval 14:43:10–14:46:50 UT enclosed by the vertical time bars (and also earlier, 14:39–14:41 UT) indicate cold  $\text{O}^+$  and  $\text{He}^+$  presence. The total densities of other ambient ions fluctuate but remain similar with and without flows, suggesting their total energies are high enough to be measured without flows. The spacecraft potential was actively controlled (Torkar et al., 2016) to  $\sim 4$  V throughout the interval.

Densities and parallel and perpendicular temperatures of cold and hot ion components (energy ranges for calculations defined in Table 1) were recalculated using the full particle distributions data during the AFM subinterval 14:43:33–14:44:33 UT using Space Physics Environment Data Analysis Software (SPEDAS) (Angelopoulos et al., 2019). The  $\text{H}^+$  energy fluxes from Energetic Ion Spectrometer (Mauk et al., 2016) were reviewed for additional energetic  $\text{H}^+$  (up to  $\sim 200$  keV) not captured by HPCA and an additional component at higher energies was not evident (not shown). The anisotropy calculated from HPCA moments was therefore used for modeling discussed in section 3. Table 1 summarizes the average of each HPCA ion components' (including the hot particles, whose energy fluxes remained nearly constant throughout the interval) moments for application to modeling. All hot plasmas had perpendicular temperature greater than parallel temperature ( $T_{\text{perp}} > T_{\text{par}}$ ), whereas the cold plasmas all featured  $T_{\text{perp}} < T_{\text{par}}$ . The  $T_{\text{perp}} < T_{\text{par}}$  of the cold

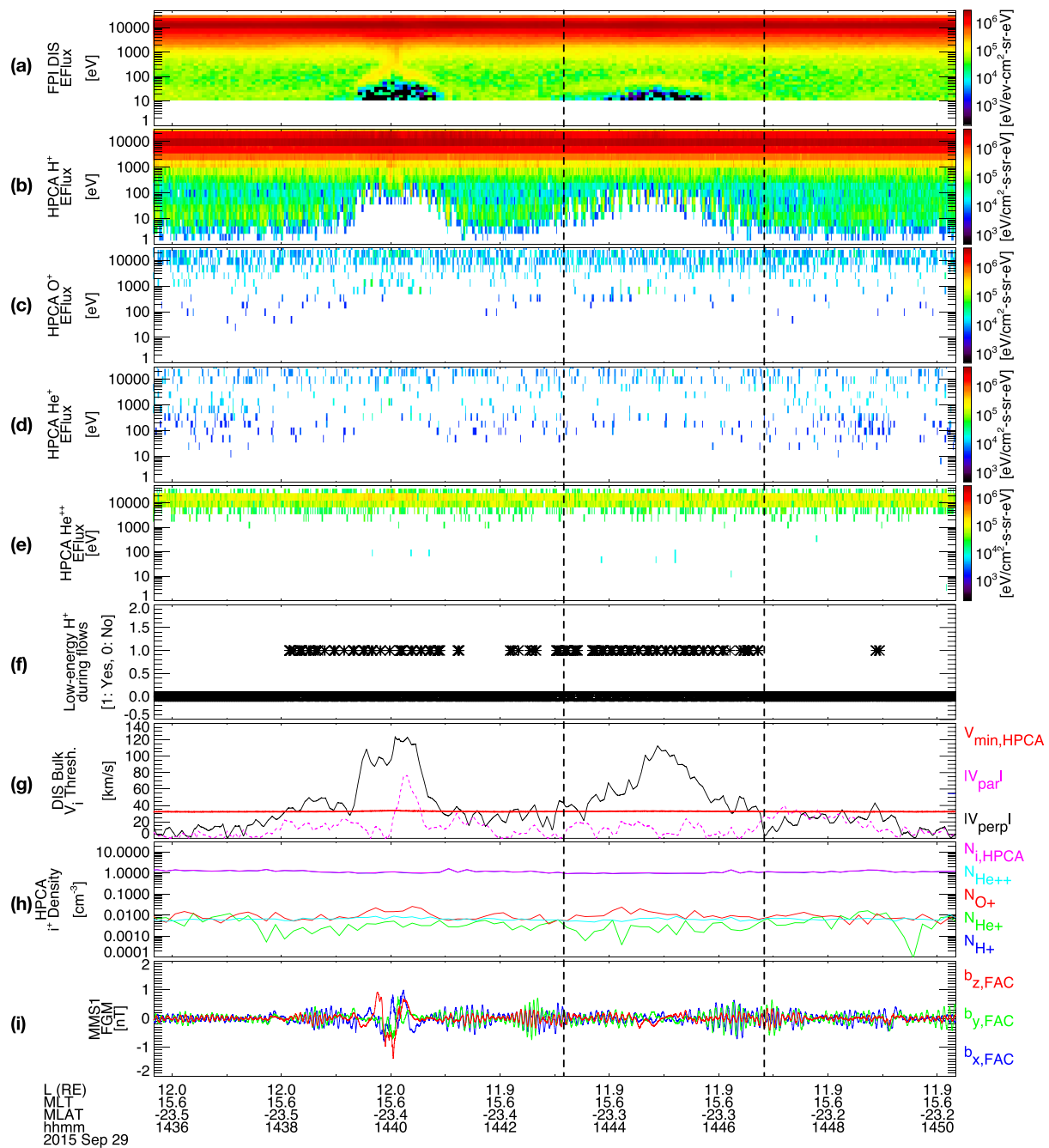


**Figure 1.** MMS-1 energy flux spectra from (a) FPI, HPCA (b)  $\text{H}^+$ , (c)  $\text{O}^+$ , (d)  $\text{He}^+$ , (e)  $\text{He}^{++}$ , (f) AFM detection intervals, (g) bulk flows with minimum HPCA velocity, (h) multi-ion densities, and (i) mean field-aligned coordinates perturbation magnetic field. Dashed vertical time bars indicate the AFM interval. MMS = Magnetospheric Multiscale; FGM = fluxgate magnetometer; MLT = magnetic local time; FAC = field-aligned coordinate; HPCA = Hot Plasma Composition Analyzer; FPI = Fast Plasma Investigation; DIS = Dual Ion Spectrometers.

plasmas is likely a consequence of ionospheric/cusp outflows at high latitudes slowly filling the volume of closed flux tubes during a period of northward IMF (Fuselier et al., 1989; Bouhram et al., 2004; Fuselier et al., 2019) and likely include warm plasma cloak ions (Chappell et al., 2008; Nosé et al., 2015).

## 2.2. Waves

Survey-mode (8 S/s) fluxgate magnetometer (FGM; Russell, Anderson, et al., 2016; Torbert et al., 2016) and fast-mode (16 S/s) EDP data were used for EMIC wave analysis. EDP data were down-sampled to match

**Table 1**  
Plasma Parameters Derived From HPCA Data Between 14:43:33  
and 14:44:33 UT for Wave Modeling Applications

Component	Species (energy range)	$n_s$ (cm <sup>-3</sup> ) <sup>a</sup>	$T_{\text{par}}$ (eV) <sup>b</sup>	$T_{\text{perp}}$ (eV)
1	H <sup>+</sup> cold (0–500 eV) <sup>c</sup>	1.87E-01	9	6
2	H <sup>+</sup> hot (500 eV–40 keV) <sup>c</sup>	8.16E-01	4296	6,134
3	He <sup>+</sup> cold (0–2,300 eV)	2.40E-03	59	50
4	He <sup>+</sup> hot (2,300 eV–40 keV)	6.73E-04	2970	6,249
5	O <sup>+</sup> cold (0–2,300 eV)	8.40E-03	39	23
6	O <sup>+</sup> hot (2,300 eV–40 keV)	5.76E-03	4264	7,889
7	He <sup>++</sup> (1–40 keV)	5.78E-03	7245	10,099
8	e <sup>-</sup>	1.026E+00 <sup>d</sup>	1	1

<sup>a</sup>The Gary (1993) method utilizes the ratio of the local Alfvén speed (calculated using the sum of combined ion mass densities, that is,  $M1 * n_{s1} + \dots + M7 * n_{s7}$ ) to light speed ( $3E+8$  [m/s]). <sup>b</sup>Ion thermal velocity for the Gary (1993) and WHAMP methods is calculated from the hot proton component's (i.e., Component 2) parallel temperature (in [K]) using the most probable thermal speed in three dimensions, that is,  $V_{\text{th}} = (2 * q * T_{\text{par}} / m_s)^{1/2}$  where  $q$  is elementary charge,  $T_{\text{par}}$  is the hot proton parallel temperature in [K] and  $m_s$  is the mass of protons in [kg]. <sup>c</sup> $k_{\parallel}$  axis in Figure 3 is calculated using the sum of cold and hot protons to represent ion density in the ion plasma frequency, that is,  $n_{s1} + n_{s2} = 1.003$  [cm<sup>-3</sup>]. <sup>d</sup>For WHAMP, the total electron number density must equal the total ion number density.

FGM data time resolution. The FGM and EDP data were transformed from the geocentric solar ecliptic coordinate system into a mean field-aligned coordinate system using standard coordinate transformation procedures (cf. Lee & Angelopoulos, 2014a). Transformed FGM and EDP data were applied to calculate wave power, Poynting vector, and magnetic field polarization spectra (Figures 2a–2e) using established wave analysis methods (cf. Lee & Angelopoulos, 2014a, and references therein); only highly polarized, coherent spectra ( $P^2 > 0.7$ ) with wave power  $> 0.01$  nT<sup>2</sup>/Hz are plotted. Local cyclotron frequencies of He<sup>+</sup>, He<sup>++</sup>, and H<sup>+</sup> are overplotted on all wave analysis spectra.

Two patches of wave emissions are enclosed within vertical time bars superposed across Figures 2a–2e. The first wave patch between 14:43:10 and 14:44:30 UT displays emissions just above and across  $f_{\text{He}+}$  but clearly below  $f_{\text{He}++}$  (Figures 2a and 2b). Poynting vector angle (Figure 2c:  $\theta_s$ ) and wave normal angle (Figure 2d:  $\theta_{\text{WNA}}$ ) data show near-field-aligned angles at and across  $f_{\text{He}+}$  and increasingly oblique angles with increasing wave emission frequency (i.e.,  $\theta_s > 60^\circ$  and  $\theta_{\text{WNA}} > 45^\circ$  at  $f_{\text{wave}} \approx 0.15$  Hz). Starting again at  $f_{\text{wave}} \approx f_{\text{He}+}$ , wave ellipticity data (Figure 2e:  $\epsilon$ ) are  $\approx 0$ , that is, linear and right-hand polarized emissions.  $\theta_s$  and  $\theta_{\text{WNA}}$  agreement suggests the packet(s) is propagating in the same direction and the polarization estimate unaffected by superposition (cf. Anderson et al., 1996; Denton et al., 1996; Lee & Angelopoulos, 2014a).  $\epsilon \gtrsim 0$  emissions can evolve following wave propagation and mode conversion enabled by plasma containing ion species in addition to protons that form crossover frequencies, discussed in section 3.

The second patch of emissions between 14:45 and 14:46:50 UT appears at higher frequency between  $f_{\text{He}+}$  and  $f_{\text{He}++}$ . Multiple wave packet presence is evident: whereas  $\theta_{\text{WNA}} \lesssim 20^\circ$  (Figure 2d),  $150^\circ \lesssim \theta_s \lesssim 50^\circ$  indicates bidirectionality (Figure 2c). In addition,  $\epsilon \approx 0$  (Figure 2e) in the same frequency range where  $\theta_s \gtrsim 150^\circ$ , consistent with superposition (Anderson, Denton, & Fuselier, 1996; Denton et al., 1996; Lee & Angelopoulos, 2014a), discussed in section 3. In general, both patches of emissions indicate quasi-field aligned propagation of wave energy in the He<sup>++</sup> band. From the satellite position data (bottom axis Figures 1 and 2), MMS-1 was located below the nominal magnetic equator so that the waves were mostly propagating toward the equator; this suggests a wave generation source at off-equatorial  $B$ -minima (Shabansky, 1971; McCollough et al., 2012; Allen et al., 2013, 2016; Vines et al., 2019), which is supported by Figure 2f showing T96 model magnetic fields (Tsyganenko & Stern, 1996) local to MMS (black line) and at the magnetic equator (red line). The field magnitude from MMS-1 (Figure 2f, blue line) fluctuated near or below both T96 fields, suggesting MMS-1 was between the equator and an off-equatorial source region.

An added capability of multisatellite missions is derivation of wave vector  $\mathbf{k}$  through phase differencing, enabling direct comparison to linear theory. We used methods described by Balikhin et al. (2003), Pinçon and Glassmeier (2008), Allen et al. (2013), and Turner et al. (2017) to calculate  $\mathbf{k}$  using the phase difference in wave magnetic field fluctuations observed across MMS spacecraft during the time intervals containing the first and second wave patches (14:43:10–14:44:30 and 14:45–14:46:50 UT). To keep results presentation focused on the  $\mathbf{k}$  estimates and their applications, multisatellite waveform data resembling Figure 1i are omitted from the figures and included with the phase differencing and wave vector calculations descriptions in the supporting information. The following  $\mathbf{k}_i$  of each wave patch were calculated:  $\mathbf{k}_1$  [ $\mathbf{k}_{1,\text{perp},\text{radial}}$ ,  $\mathbf{k}_{1,\text{perp},\text{azimuthal}}$ ,  $\mathbf{k}_{1,\parallel}$ ] =  $[11.9, -3.5, 8.5] \times 1E-4 \pm [1.2, -0.2, 1.3] \times 1E-4$  rad/km and  $\mathbf{k}_2 = [2.6, -3.0, 12.6] \times 1E-4 \pm [0.8, -0.2, 1.0] \times 1E-4$  rad/km, where the error bars are the standard deviation around the mean wave vector calculated from all spacecraft pairs. Wave normal angle of each  $\mathbf{k}_i$  relative to the average field is calculated from the arc-cosine of the ratio of  $\mathbf{k}_{i,\parallel}$  to  $|\mathbf{k}_i|$ :  $\theta_{k,1} \approx 57^\circ$  and  $\theta_{k,2} \approx 17^\circ$ .  $\theta_{k,1}$  and  $\theta_{k,2}$  are consistent with Figures 2c and 2d. Note, however, that  $\mathbf{k}_i$  and  $\theta_{k,i}$  estimates include multiple wave packets emitted at the same frequency but which may be propagating in multiple directions. At present, there is not a way to



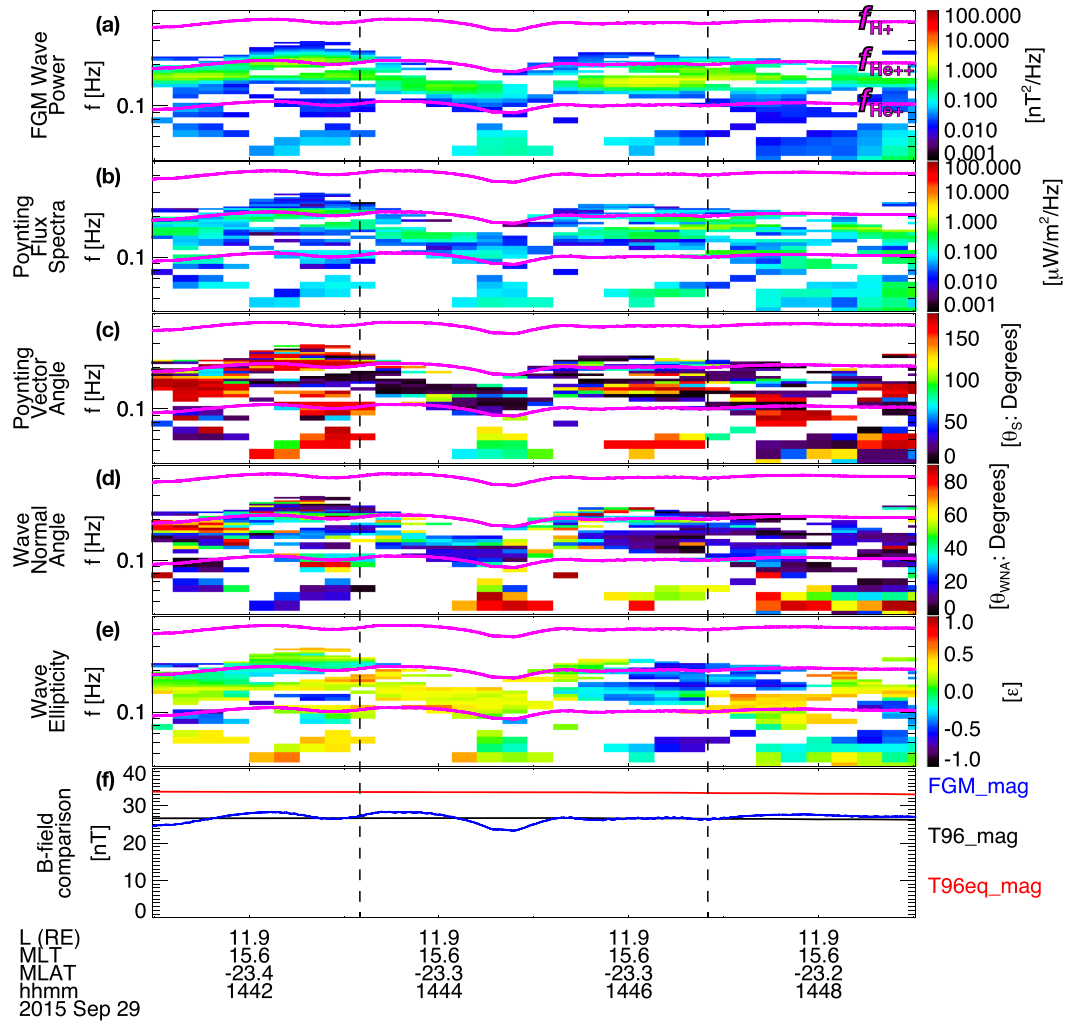


**Figure 2.** MMS-1 (a) wave power spectra, (b) Poynting flux spectra, (c) Poynting flux angle,  $\theta_S$ , (d) wave normal angle,  $\theta_{WNA}$ , (e) wave ellipticity,  $\epsilon$ , and (f) ambient magnetic field analysis. Dashed vertical time bars indicate the AFM interval. FGM = fluxgate magnetometer; MLT = magnetic local time.

deconvolve simultaneous wave packets, that is, superposition, from multisatellite  $\mathbf{k}$ -vector analysis. Superposition effects on analysis are discussed below.

### 3. Modeling and Discussion

Plasma data (Table 1) were applied to three independent dispersion relation solvers (Gary, 1993; Kyoto University Plasma Dispersion Analysis Package [http://space.rish.kyoto-u.ac.jp/software; cf. Sugiyama et al., 2015] and Waves in Homogeneous Anisotropic Magnetized Plasma [WHAMP; https://github.com/irfu/whamp; cf. Rönnmark, 1982]) for modeling, with similar results obtained from all. Gary (1993) was used to produce results in Figure 3 and Rönnmark (1982) was used to produce results in Figure 4.

Figures 3a–3c show results using as-measured parameters and Figures 3d–3f show results with added anisotropy (from  $A = 0.43$  as-measured to  $A = 0.9$ ) using the relation between observed wave frequency and critical anisotropy (i.e.,  $f_c = f_{H+}[A/(A + 1)]$ ) relating critical wave frequency  $f_c$  normalized to the proton cyclotron frequency  $f_{H+}$  to hot proton anisotropy  $A$ , where  $A = T_{\text{perp}}/T_{\text{par}} - 1$ ; Kennel & Petschek, 1966). Figure 3a1 (3d1) shows the solutions relating normalized wave frequency,  $\omega/\Omega_{H+}$ , and normalized wave vector,  $\mathbf{k}c/\omega_{pH+}$  ( $c$  is light speed and  $\omega_{pH+}$  is the proton plasma frequency), and (Figures 3a2 and 3d2) their normalized growth rates,  $\gamma/\Omega_{H+}$ , for all parallel-propagating modes including the right-handed whistler mode that helps define the crossover frequencies. The as-measured parameters produced no wave growth,

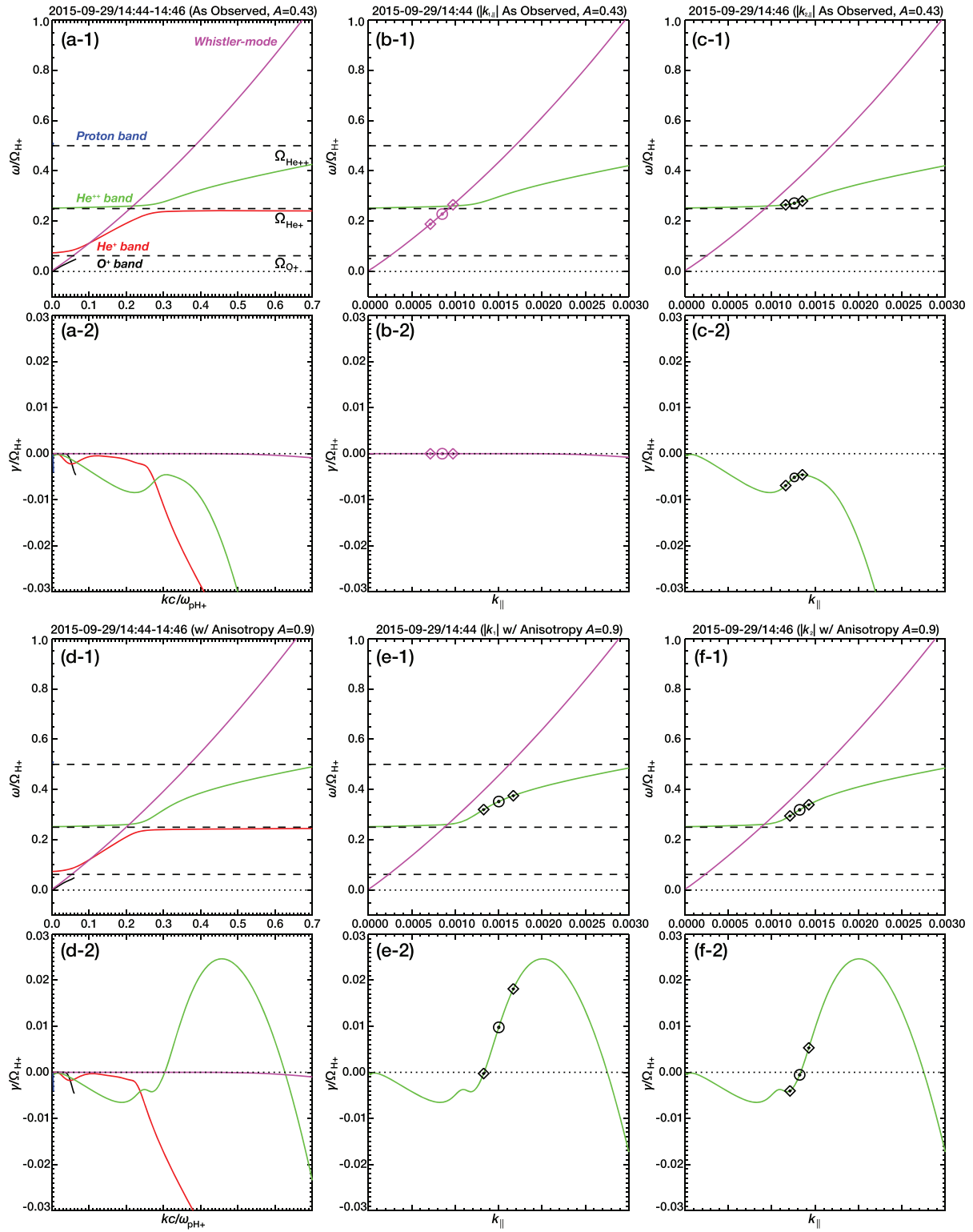


**Figure 3.** Dispersion relation solutions showing (a1)  $\omega/\Omega_{H^+}$  versus  $kc/\omega_{pH^+}$  for left-handed EMIC modes (black:  $O^+$  band, red:  $He^+$  band, green:  $He^{++}$  band, blue:  $H^+$  band) and right-handed whistler-mode (magenta) using as-measured plasma parameters and (a2) their corresponding  $\gamma/\Omega_{H^+}$ ; (b1)  $|k_{||}|$  (circle) and errors (diamonds) (c1)  $|k_{\perp}|$  (circle) and errors (diamonds) derived through multispacecraft data over-plotted onto  $\omega/\Omega_{H^+}$  versus  $k_{||}$  and corresponding  $\gamma/\Omega_{H^+}$  (b2 and c2). (d1) combined solutions showing  $\omega/\Omega_{H^+}$  versus  $kc/\omega_{pH^+}$  for left-handed EMIC modes (labeled and colored as a1) and right-handed whistler-mode (magenta) using same plasma parameters except for increased hot proton anisotropy to 0.9 and (d1) corresponding  $\gamma/\Omega_{H^+}$ ; (e1)  $|k_{||}|$  (circle) and errors (diamonds) (f1)  $|k_{\perp}|$  (circle) and errors (diamonds) derived through multispacecraft data overplotted onto  $\omega/\Omega_{H^+}$  versus  $k_{||}$  and corresponding  $\gamma/\Omega_{H^+}$  (e2 and f2).

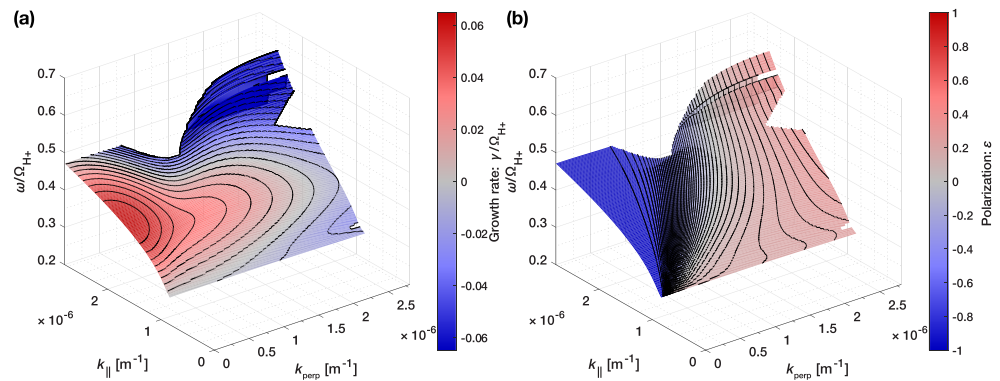


**Figure 4.** WHAMP surfaces including contours showing (a) relation between  $\omega/\Omega_{H^+}$  and  $k$  from parallel ( $0^\circ$ ) to oblique ( $90^\circ$ ) wave angles for increased anisotropy with color scale showing the normalized growth rates,  $\gamma/\Omega_{H^+}$ ; (b) wave polarization ( $\epsilon$ ) calculated from the modeled wave fields. Regions without converging solutions or with severely damped solutions are masked.

suggesting the plasma was marginally stable—not unexpected since the observations showed wave propagation. Figures 3b1, 3c1, 3e1, and 3f1 show two branches of the solutions from Figure 3a1 or 3d1, except plotted as the relation between  $\omega/\Omega_{H^+}$  and nonnormalized  $k_{||}$ ;  $k_{||}$  was calculated using the total (cold and hot) proton density in Table 1 for  $\omega_{pH^+}$ . The critical frequencies ( $f_c/f_{H^+} \sim 0.33\text{--}0.46$ ) used to calculate a hot proton anisotropy range ( $A \sim 0.5\text{--}0.9$ ) were informed by the frequencies of peak wave power (derived from Figure 2a); the wave power peaks served as midpoints for the full emission range and provided a conservative  $A$  range for modeling. Comparing Figures 3a to 3d, setting  $A = 0.9$  results in only  $\text{He}^{++}$  band waves being unstable (Figures 3d1 and 3d2), consistent with sustained wave emissions above  $f_{\text{He}^+}$  and below  $f_{\text{He}^{++}}$  seen in the observations.  $A = 0.9$  is less than what Anderson et al. (1992 and Anderson, Denton, Ho, et al., 1996) reported was needed to excite EMIC waves along dawn to early afternoon MLT at  $L > 7 R_E$  ( $A > 1.0$  and as high as  $\sim 2.3$ ). Participation of cold and hot  $\text{O}^+$ , cold and hot  $\text{He}^+$ , and solar wind  $\text{He}^{++}$  in wave growth and formation of more frequency bands and another crossover frequency just above  $\Omega_{\text{He}^+}$  in the  $\text{He}^{++}$  band ( $\Omega_{\text{coHe}^{++}}$ ) were not discussed by Anderson, Denton, Ho, et al., 1996; also Anderson & Fuselier, 1994 due to the cold ions having energies below the spacecraft potential; investigations focused on fitted cold  $\text{H}^+$  and  $\text{He}^+$  and hot  $\text{H}^+$ ,  $\text{He}^+$ , and  $\text{He}^{++}$  during wave activity. It was seen through modeling (additional cases using combinations of Table 1 parameters included in supporting information) that in addition to  $\text{He}^+$  and  $\text{H}^+$ ,  $\text{O}^+$  components are needed to (1) obtain positive growth when  $A = 0.9$  in a  $k\omega/\omega_{pH^+}$  range consistent with Figure 3d and the  $f/f_{H^+}$  range in Figure 2a and (2) form the crossover frequency above  $\Omega_{\text{He}^+}$ . As for  $\text{He}^{++}$ , even though a similar unstable  $k\omega/\omega_{pH^+}$  range appeared when any heavy ion components accompanied  $\text{H}^+$ , wave damping in the  $\text{He}^{++}$  band (Figure 3d1) near  $\Omega_{\text{He}^{++}}$  is consistent with low wave power near  $f_{\text{He}^{++}}$  (Figure 2a) and could partially explain heating of  $\text{He}^{++}$  exceeding  $\text{H}^+$ , as was modeled in the solar wind (Gomberoff et al., 1996). Improved modeling and data agreement suggest future studies should apply methods (e.g., section 2.1) to ensure measurement of cold and hot plasma composition or develop improved instrumentation (Zurbuchen & Gershman, 2016) to accurately characterize magnetospheric composition and assess effects on EMIC waves. Realistic, complex composition data could be used in sophisticated wave modeling applications to also investigate composition effects on wave propagation (e.g., Kim et al., 2019) or the waves' effectiveness in energetic particle scattering (e.g., Denton et al., 2019).

MMS-derived  $k_i$  from wave patch 1 ( $k_1$ ) was applied to test the modeling, starting with its parallel component. Although wave patch 2 ( $k_2$ ) was also applied to the same tests (cf. Figures 3c and 3f), discussion focuses on the effects of superposition on those test results. Figure 3b shows  $k_{1,||}$  plotted onto the whistler-mode branch. Recall  $k_1$  had oblique wave normal angle above  $f_{\text{He}^+}$  ( $\theta_s$  [Figure 2c],  $\theta_{\text{WNA}}$  [Figure 2d], and  $\theta_{k,1}$  all  $> 30^\circ$ ) and  $\epsilon \gtrsim 0$  (Figure 2e) but was quasi-field aligned near  $f_{\text{He}^+}$ . Consistent with descriptions by Thorne et al. (2013), the wave normal angle and near-linear polarization of wave patch 1 above  $f_{\text{He}^+}$  suggest the emissions were near  $\Omega_{\text{coHe}^{++}}$  whereas the portion of the emissions on and crossing  $f_{\text{He}^+}$  with  $\epsilon > 0$  may have been converted to right-handed (whistler-mode branch) after propagating across  $\Omega_{\text{coHe}^{++}}$ .  $k_{1,||}$  (circle)



and its error bars (diamonds) are thus plotted on the whistler-mode branch (Figure 3b1), where it agrees well with the model:  $k_{1,\parallel}$  is to the left of  $\Omega_{\text{coHe}^{++}}$  (point where LH and RH branches cross in  $\text{He}^{++}$  band). Furthermore,  $k_{1,\parallel}$  crosses  $\Omega_{\text{He}^+}$  ( $\omega/\Omega_{\text{He}^+} = 0.25$ ), consistent with  $\varepsilon > 0$  emissions on  $f_{\text{He}^+}$  (Figure 2e).

$k_1$  was also applied to the unstable  $\text{He}^{++}$  band wave modeling, where it was assumed to retain properties immediately following generation so that  $|k_1|$  (vector magnitude) was a fully parallel-propagating packet, that is,  $|k_{1,\parallel}| = |k_1|$ .  $|k_{1,\parallel}|$  is plotted on Figure 3e, where it lies directly on the positive growing portion of the  $\text{He}^{++}$  band (Figure 3e2). Now revisiting the effects of superposition on validity of multisatellite  $k$  determination, Figure 3f2 shows  $|k_{2,\parallel}|$  on a weakly growing portion of the  $\text{He}^{++}$  band (also see Figure 3c1 showing  $k_{2,\parallel}$  at  $\omega/\Omega_{\text{He}^+} < 0.3$ , which is below peak wave power at  $f/f_{\text{He}^+} \sim 0.35$  seen in the data). Assuming linear theory holds, observation that  $|k_{2,\parallel}|$  does not lie on a strongly growing portion of the  $\text{He}^{++}$  branch suggests some factor reduces the multispacecraft-derived  $k_i$ . This can be understood by considering that two wave packets with equal properties propagating in opposite directions should result in  $k_i$  of zero. The fact that  $k_2$  is not zero suggests a dominant propagation direction to patch 2 emissions. But what portion(s) of  $k_2$ 's properties are lost due to superposition cannot be determined. Testing  $k_2$  to theory shows how multispacecraft analysis can be limited by superposition. The superposition signatures ( $\theta_{\text{WNA}} \lesssim 20^\circ$  (Figure 2d),  $150^\circ \lesssim \theta_s \lesssim 50^\circ$  indicating bi-directionality (Figure 2c), and  $\varepsilon \approx 0$  (Figure 2e) in the same frequency range where  $\theta_s \gtrsim 150^\circ$ ) combined with modeling suggest  $k_2$  is an underestimate. Had  $k_2$  been derived from a single wave packet, then it may have appeared in a  $k$  range of greater instability. Superposition may also affect patch 1 but likely to a lesser degree than interpreted for patch 2.

The modeling has focused on parallel modes due to their expectation of strongest growth (Gary et al., 2012). But Denton et al. (1992) noted oblique, linear-polarized modes could be preferentially generated in the day-side region. Data were also applied to explore these modes. Energetic protons with a loss cone-like distribution were not seen in 2-D cuts of the ion distribution functions (FPI/DIS and HPCA  $\text{H}^+$  data were consulted, shown in the supporting information) so a bi-Maxwellian hot proton distribution with temperature anisotropy ( $A = 0.9$ ) was used for modeling of  $\text{He}^{++}$  band waves over a range of  $\theta_{\text{WNA}}$  from  $0^\circ$  to  $90^\circ$ . The  $\text{He}^{++}$  band dispersion surfaces and contours in Figure 4a show that  $\gamma/\Omega_{\text{He}^+} > 0$  at  $\theta_{\text{WNA}} > 0^\circ$  (i.e., as  $k_{\text{perp}}$  increases for  $k_{\parallel}$  above  $\sim 1.5 \times 10^{-6} \text{ m}^{-1}$ ) and peak  $\gamma/\Omega_{\text{He}^+}$  occurs for  $\theta_{\text{WNA}} = 0^\circ$  waves, with  $\gamma/\Omega_{\text{He}^+}$  decreasing with increasing  $\theta_{\text{WNA}}$  and  $\varepsilon$  (Figure 4b). So, although linear polarized modes have smaller growth rate than left-handed modes, linear waves could still grow with sufficient free energy.

## 4. Conclusions

MMS ion composition measurements during fast flows enabled detailed investigation of EMIC waves with properties consistent with what have been described as peculiar. Past waves could have been affected by similar plasma composition containing multiple cold/heated ionospheric and solar wind ion species. Solar wind ions can have comparable abundances to ionospheric-originating ions in the outer magnetosphere (Allen et al., 2016; Cohen et al., 2017), where  $\text{He}^{++}$  band waves have been observed (Engebretson et al., 2018). Investigations of MMS data when cold and hot plasmas are fully measurable in the inner magnetosphere or other MLT sectors will improve knowledge on competing influences of ionospheric and solar wind plasma sources and effects on EMIC waves (e.g., Miyoshi et al., 2019). Such investigations could support studies on ion composition impacts on magnetic reconnection or its variability near or within the plasmasphere and warm plasma cloak.

## References

- Allen, R. C., Livi, S. A., & Goldstein, J. (2016). Variations of oxygen charge state abundances in the global magnetosphere, as observed by Polar. *Journal of Geophysical Research: Space Physics*, 121, 1091–1113. <https://doi.org/10.1002/2015JA021765>
- Allen, R. C., Zhang, J.-C., Kistler, L. M., Spence, H. E., Lin, R.-L., Dunlop, M. W., & André, M. (2013). Multiple bidirectional EMIC waves observed by Cluster at middle magnetic latitudes in the dayside magnetosphere. *Journal of Geophysical Research: Space Physics*, 118, 6266–6278. <https://doi.org/10.1002/jgra.50600>
- Allen, R. C., Zhang, J.-C., Kistler, L. M., Spence, H. E., Lin, R.-L., Klecker, B., et al. (2015). A statistical study of EMIC waves observed by Cluster: 1. Wave properties. *Journal of Geophysical Research: Space Physics*, 120, 5574–5592. <https://doi.org/10.1002/2015JA021333>
- Allen, R. C., Zhang, J.-C., Kistler, L. M., Spence, H. E., Lin, R.-L., Klecker, B., et al. (2016). A statistical study of EMIC waves observed by Cluster: 2. Associated plasma conditions. *Journal of Geophysical Research: Space Physics*, 121, 6458–6479. <https://doi.org/10.1002/2016JA022541>

## Acknowledgments

J. H. L. and D. L. T. acknowledge support from NASA grant 80NSSC18K1378 and thank the MMS instrument teams and program for generating measurements used in this study. MMS data are available from the MMS Science Data Center (<https://lasp.colorado.edu/mms/sdc/public/>). SPEDAS tools are available through <http://spedas.org/blog/> website. The solar wind and Dst data were provided by NASA SPDF OMNIWeb (<https://omniweb.gsfc.nasa.gov/>) and the WDC for Geomagnetism, Kyoto (<http://wdc.kugi.kyoto-u.ac.jp/wdc/Sec3.html>), respectively.

- Anderson, B. J., Denton, R. E., & Fuselier, S. A. (1996). On determining polarization characteristics of ion cyclotron wave magnetic field fluctuations. *Journal of Geophysical Research*, 101(A6), 13,195–13,213. <https://doi.org/10.1029/96JA00633>
- Anderson, B. J., Denton, R. E., Ho, G., Hamilton, D. C., Fuselier, S. A., & Strangeway, R. J. (1996). Observational test of local proton cyclotron instability in the Earth's magnetosphere. *Journal of Geophysical Research*, 101(A10), 21,527–21,543. <https://doi.org/10.1029/96JA01251>
- Anderson, B. J., Erlanson, R. E., & Zanetti, L. J. (1992). A statistical study of Pc 1–2 magnetic pulsations in the equatorial magnetosphere: 2. Wave properties. *Journal of Geophysical Research*, 97(A3), 3089–3101. <https://doi.org/10.1029/91JA02697>
- Anderson, B. J., & Fuselier, S. A. (1994). Response of thermal ions to electromagnetic ion cyclotron waves. *Journal of Geophysical Research*, 99(A10), 19,413–19,425. <https://doi.org/10.1029/94JA01235>
- André, M., & Cully, C. M. (2012). Low-energy ions: A previously hidden solar system particle population. *Geophysical Research Letters*, 39, L03101. <https://doi.org/10.1029/2011GL050242>
- Angelopoulos, V. (2008). The THEMIS Mission. *Space Science Reviews*, 141(1–4), 5–34. <https://doi.org/10.1007/s11214-008-9336-1>
- Angelopoulos, V., Cruce, P., Drozdov, A., Grimes, E. W., Hatzigeorgiu, N., King, D. A., et al. (2019). *Space Science Reviews*, 215(1), 9. <https://doi.org/10.1007/s11214-018-0576-4>
- Balikhin, M. A., Pokhotelov, O. A., Walker, S. N., Amata, E., Andre, M., Dunlop, M., & Alleyne, H. S. C. K. (2003). Minimum variance free wave identification: Application to Cluster electric field data in the magnetosheath. *Geophysical Research Letters*, 30(10), 1508. <https://doi.org/10.1029/2003GL016918>
- Bouhram, M., Klecker, B., Miyake, W., Rème, H., Sauvaud, J.-A., Malingre, M., et al. (2004). On the altitude dependence of transversely heated O<sup>+</sup> distributions in the cusp/cleft. *Annales de Geophysique*, 22, 1787–1798. <https://doi.org/10.5194/angeo-22-1787-2004>
- Burch, J. L., Moore, T. E., Torbert, R. B., & Giles, B. L. (2016). Magnetospheric Multiscale overview and science objectives. *Space Science Reviews*, 199(1–4), 5–21. <https://doi.org/10.1007/s11214-015-0164-9>
- Chappell, C. R., Huddleston, M. M., Moore, T. E., Giles, B. L., & Delcourt, D. C. (2008). Observations of the warm plasma cloak and an explanation of its formation in the magnetosphere. *Journal of Geophysical Research*, 113, A09206. <https://doi.org/10.1029/2007JA012945>
- Chen, L., Thorne, R. M., & Bortnik, J. (2011). The controlling effect of ion temperature on EMIC wave excitation and scattering. *Geophysical Research Letters*, 38, L16109. <https://doi.org/10.1029/2011GL048653>
- Chen, S.-H., & Moore, T. E. (2004). Dayside flow bursts in the Earth's outer magnetosphere. *Journal of Geophysical Research*, 109, A03215. <https://doi.org/10.1029/2003JA010007>
- Cohen, I. J., Mitchell, D. G., Kistler, L. M., Mauk, B. H., Anderson, B. J., Westlake, J. H., et al. (2017). Dominance of high-energy (>150 keV) heavy ion intensities in Earth's middle to outer magnetosphere. *Journal of Geophysical Research: Space Physics*, 122, 9282–9293. <https://doi.org/10.1002/2017ja024351>
- Denton, R. E., Anderson, B. J., Ho, G., & Hamilton, D. C. (1996). Effects of wave superposition on the polarization of electromagnetic ion cyclotron waves. *Journal of Geophysical Research*, 101(A11), 24,869–24,885. <https://doi.org/10.1029/96JA02251>
- Denton, R. E., Hudson, M. K., & Roth, I. (1992). Loss-cone-driven ion cyclotron waves in the magnetosphere. *Journal of Geophysical Research*, 97(A8), 12093–12103. <https://doi.org/10.1029/92JA00954>
- Denton, R. E., Ofman, L., Shprits, Y. Y., Bortnik, J., Millan, R. M., Rodger, C. J., et al. (2019). Pitch angle scattering of sub-MeV relativistic electrons by electromagnetic ion cyclotron waves. *Journal of Geophysical Research: Space Physics*, 124(7), 5610–5626. <https://doi.org/10.1029/2018JA026384>
- Engebretson, M. J., Posch, J. L., Capman, N. S. S., Campuzano, N. G., Bèlik, P., Allen, R. C., et al. (2018). MMS, Van Allen Probes, GOES 13, and ground-based magnetometer observations of EMIC wave events before, during, and after a modest interplanetary shock. *Journal of Geophysical Research: Space Physics*, 123(10), 8331–8357. <https://doi.org/10.1029/2018JA025984>
- Ergun, R. E., Tucker, S., Westfall, J., Goodrich, K. A., Malaspina, D. M., Summers, D., et al. (2016). *Space Science Reviews*, 199(1–4), 167–188. <https://doi.org/10.1007/s11214-014-0115-x>
- Fuselier, S. A., Klumpp, D. M., Peterson, W. K., & Shelley, E. G. (1989). Direct injection of ionospheric O<sup>+</sup> into the dayside low latitude boundary layer. *Geophysical Research Letters*, 16(10), 1121–1124. <https://doi.org/10.1029/GL016i010p01121>
- Fuselier, S. A., Trattner, K. J., Petriner, S. M., Denton, M. H., Toledo-Redondo, S., André, M., et al. (2019). Mass loading the Earth's dayside magnetopause boundary layer and its effect on magnetic reconnection. *Geophysical Research Letters*, 46(12), 6204–6213. <https://doi.org/10.1029/2019GL082384>
- Gary, S. (1993). *Theory of space plasma microinstabilities (Cambridge Atmospheric and Space Science Series)*. Cambridge: Cambridge University Press. <https://doi.org/10.1017/CBO9780511551512>
- Gary, S. P., Liu, K., & Chen, L. (2012). Alfvén-cyclotron instability with singly ionized helium: Linear theory. *Journal of Geophysical Research*, 117, A08201. <https://doi.org/10.1029/2012JA017740>
- Gomberoff, L., Gratton, F. T., & Gnani, G. (1996). Acceleration and heating of heavy ions by circularly polarized Alfvén waves. *Journal of Geophysical Research*, 101(A7), 15,661–15,665. <https://doi.org/10.1029/96JA00684>
- Kennel, C. F., & Petschek, H. E. (1966). Limit on stably trapped particle fluxes. *Journal of Geophysical Research*, 71(1), 1–28. <https://doi.org/10.1029/JZ071i001p00001>
- Kim, E.-H., Johnson, J. R., & Lee, D.-H. (2019). Electron inertial effects on linearly polarized electromagnetic ion cyclotron waves at Earth's magnetosphere. *Journal of Geophysical Research: Space Physics*, 124, 2643–2655. <https://doi.org/10.1029/2019JA026532>
- Le, G., Blanco-Cano, X., Russell, C. T., Zhou, X. -W., Mozer, F., Trattner, K. J., et al. (2001). Electromagnetic ion cyclotron waves in the high-altitude cusp: Polar observations. *Journal of Geophysical Research*, 106(A9), 19067–19079. <https://doi.org/10.1029/2000JA900163>
- Lee, J. H., & Angelopoulos, V. (2014a). Observations and modeling of EMIC wave properties in the presence of multiple ion species as function of magnetic local time. *Journal of Geophysical Research: Space Physics*, 119, 8942–8970. <https://doi.org/10.1002/2014JA020469>
- Lee, J. H., & Angelopoulos, V. (2014b). On the presence and properties of cold ions near Earth's equatorial magnetosphere. *Journal of Geophysical Research: Space Physics*, 119, 1749–1770. <https://doi.org/10.1002/2013JA019305>
- Lee, J. H., Chen, L., Angelopoulos, V., & Thorne, R. M. (2012). THEMIS observations and modeling of multiple ion species and EMIC waves: Implications for a vanishing He<sup>+</sup> stop band. *Journal of Geophysical Research*, 117, A06204. <https://doi.org/10.1029/2012JA017539>
- Lindqvist, P. A., Olsson, G., Torbert, R. B., King, B., Granoff, M., Rau, D., & Tucker, S. (2016). The spin-plane double probe electric field instrument for MMS. *Space Science Reviews*, 199(1–4), 137–165. <https://doi.org/10.1007/s11214-014-0116-9>
- Mauk, B. H., Blake, J. B., Baker, D. N., Clemmons, J. H., Reeves, G. D., Spence, H. E., et al. (2016). *Space Science Reviews*, 199(1–4), 471–514. <https://doi.org/10.1007/s11214-014-0055-5>

- McCollough, J. P., Elkington, S. R., & Baker, D. N. (2012). The role of Shabansky orbits in compression-related electromagnetic ion cyclotron wave growth. *Journal of Geophysical Research*, 117, A01208. <https://doi.org/10.1029/2011JA016948>
- Min, K., Lee, J., Keika, K., & Li, W. (2012). Global distribution of EMIC waves derived from THEMIS observations. *Journal of Geophysical Research*, 117, A05219. <https://doi.org/10.1029/2012JA017515>
- Miyoshi, Y., Matsuda, S., Kurita, S., Nomura, K., Keika, K., Shoji, M., et al. (2019). EMIC waves converted from equatorial noise due to  $M/Q = 2$  ions in the plasmasphere: Observations from Van Allen Probes and Arase. *Geophysical Research Letters*, 46, 5662–5669. <https://doi.org/10.1029/2019GL083024>
- Nosé, M., Oimatsu, S., Keika, K., Kletzing, C. A., Kurth, W. S., Pascuale, S. D., et al. (2015). Formation of the oxygen torus in the inner magnetosphere: Van Allen Probes observations. *Journal of Geophysical Research: Space Physics*, 120, 1182–1196. <https://doi.org/10.1002/2014JA020593>
- Omidi, N., Bortnik, J., Thorne, R., & Chen, L. (2013). Impact of cold  $O^+$  ions on the generation and evolution of EMIC waves. *Journal of Geophysical Research: Space Physics*, 118, 434–445. <https://doi.org/10.1029/2012JA018319>
- Pinçon, J.-L., & Glassmeier, K.-H. (2008). Multi-spacecraft methods of wave field characterization. *ISSI Scientific Reports Series*, 8, 47–54.
- Pollock, C., Moore, T., Jacques, A., Burch, J., Gliese, U., Saito, Y., et al. (2016). *Space Science Reviews*, 199(1-4), 331–406. <https://doi.org/10.1007/s11214-016-0245-4>
- Rönmark, K. (1982). WHAMP—Waves in homogeneous, anisotropic, multicomponent plasmas, Kiruna Geophys. Inst. Rep. 179 (KGI—179), Swed. Inst. Of Space Phys., Univ. of Umea, Umea, Sweden.
- Russell, C. T., Anderson, B. J., Baumjohann, W., Bromund, K. R., Dearborn, D., Fischer, D., & Leinweber, H. K. (2016). The Magnetospheric Multiscale magnetometers. *Space Science Reviews*, 199(1-4), 189–256. <https://doi.org/10.1007/s11214-014-0057-3>
- Russell, C. T., Wei, H. Y., Cowee, M. M., Neubauer, F. M., & Dougherty, M. K. (2016). Ion cyclotron waves at Titan. *Journal of Geophysical Research: Space Physics*, 121, 2095–2103. <https://doi.org/10.1002/2015JA022293>
- Sauvaud, J.-A., Lundin, R., Rème, H., McFadden, J. P., Carlson, C., Parks, G. K., et al. (2001). Intermittent thermal plasma acceleration linked to sporadic motions of the magnetopause, first Cluster results. *Annales de Geophysique*, 19(10/12), 1523–1532. <https://doi.org/10.5194/angeo-19-1523-2001>
- Shabansky, V. P. (1971). *Space Science Reviews*, 12(3), 299–418. <https://doi.org/10.1007/BF00165511>
- Shprits, Y. Y., Drozdov, A. Y., Spasojevic, M., Kellerman, A. C., Usanova, M. E., Engebretson, M. J., et al. (2016). Wave-induced loss of ultra-relativistic electrons in the Van Allen radiation belts. *Nature Communications*, 7(1), 1–7. <https://doi.org/10.1038/ncomms12883>
- Shprits, Y. Y., Kellerman, A., Aseev, N., Drozdov, A. Y., & Michaelis, I. (2017). Multi-MeV electron loss in the heart of the radiation belts. *Geophysical Research Letters*, 44, 1204–1209. <https://doi.org/10.1002/2016GL072258>
- Silin, I., Mann, I. R., Sydora, R. D., Summers, D., & Mace, R. L. (2011). Warm plasma effects on electromagnetic ion cyclotron wave MeV electron interactions in the magnetosphere. *Journal of Geophysical Research*, 116, A05215. <https://doi.org/10.1029/2010JA016398>
- Sugiyama, H., Singh, S., Omura, Y., Shoji, M., Nunn, D., & Summers, D. (2015). Electromagnetic ion cyclotron waves in the Earth's magnetosphere with a kappa-Maxwellian particle distribution. *Journal of Geophysical Research: Space Physics*, 120, 8426–8439. <https://doi.org/10.1002/2015JA021346>
- Thorne, R. M., Horne, R. B., Jordanova, V. K., Bortnik, J., & Glauert, S. (2013). Interaction of emic waves with thermal plasma and radiation belt particles. In K. Takahashi, P. J. Chi, R. E. Denton, & R. L. Lysak (Eds.), *Magnetospheric ULF Waves: Synthesis and New Directions* (213–223 pp.). Washington, DC, USA: American Geophysical Union. <https://doi.org/10.1029/169GM14>
- Thorne, R. M., & Kennel, C. F. (1971). Relativistic electron precipitation during magnetic storm main phase. *Journal of Geophysical Research*, 76(19), 4446–4453. <https://doi.org/10.1029/JA076i019p04446>
- Torbert, R. B., Russell, C. T., Magnes, W., Ergun, R. E., Lindqvist, P.-A., LeContel, O., & Lappalainen, K. (2016). The FIELDS instrument suite on MMS: Scientific objectives, measurements, and data products. *Space Science Reviews*, 199(1-4), 105–135. <https://doi.org/10.1007/s11214-014-0109-8>
- Torkar, K., Nakamura, R., Tajmar, M., Scharlemann, C., Jeszenszky, H., Laky, G., et al. (2016). *Space Science Reviews*, 199(1-4), 515–544. <https://doi.org/10.1007/s11214-014-0049-3>
- Tsyganenko, N. A., & Stern, D. P. (1996). Modeling the global magnetic field of the large-scale Birkeland current systems. *Journal of Geophysical Research*, 101(A12), 27187–27198. <https://doi.org/10.1029/96JA02735>
- Turner, D. L., Lee, J. H., Claudepierre, S. G., Fennell, J. F., Blake, J. B., Jaynes, A. N., et al. (2017). Examining coherency scales, substructure, and propagation of whistler mode chorus elements with Magnetospheric Multiscale (MMS). *Journal of Geophysical Research: Space Physics*, 122, 11,201–11,226. <https://doi.org/10.1002/2017JA024474>
- Usanova, M. E., Drozdov, A., Orlova, K., Mann, I. R., Shprits, Y., Robertson, M. T., et al. (2014). Effect of EMIC waves on relativistic and ultrarelativistic electron populations: Ground-based and Van Allen Probes observations. *Geophysical Research Letters*, 41, 1375–1381. <https://doi.org/10.1002/2013GL059024>
- Vines, S. K., Allen, R. C., Anderson, B. J., Engebretson, M. J., Fuselier, S. A., Russell, C. T., et al. (2019). EMIC waves in the outer magnetosphere: Observations of an off-equator source region. *Geophysical Research Letters*, 46. <https://doi.org/10.1029/2019GL082152>
- Young, D. T., Burch, J. L., Gomez, R. G., Los Santos, A., Miller, G. P., Wilson, P. IV, et al. (2016). *Space Science Reviews*, 199(1-4), 407–470. <https://doi.org/10.1007/s11214-014-0119-6>
- Zurbuchen, T. H., & Gershman, D. J. (2016). Innovations in plasma sensors. *Journal of Geophysical Research: Space Physics*, 121, 2891–2901. <https://doi.org/10.1002/2016JA022493>